ARTICLE

Reaction of OH radicals with CH_3NH_2 in the gas phase: Experimental (11.7-177.5 K) and computed rate coefficients (10-1000 K)

Received 00th January 20xx,
Accepted 00th January 20xx

DOI: 10.1039/x0xx00000x

Daniel González,[a] Anxo Lema-Saavedra,[b] Sara Espinosa,[a] Emilio Martínez-Núñez,[c] Antonio Fernández-Ramos,*[bc] André Canosa,[d] Bernabé Ballesteros[ae], and Elena Jiménez *[ae]

Nitrogen-bearing molecules, like methylamine (CH_3NH_2), can be the building blocks of amino acids in the interstellar medium (ISM). At the ultralow temperatures of the ISM, it is important to know its gas-phase reactivity towards interstellar radicals and the products formed. In this work, the kinetics of the OH+CH_3NH_2 reaction was experimental and theoretically investigated at the low- and high pressure limits (LPL and HPL) between 10 and 1000 K. Moreover, the CH_2NH_2 and CH_3NH yields were computed in the same temperature range for both pressure regimes. A pulsed CRESU (French acronym for Reaction Kinetics in a Uniform Supersonic Flow) apparatus was employed to determine the rate coefficient, *k*(T), in the 11.7-177.5 K range. A drastic increase of *k*(T) as temperature is lowered was observed in agreement with theoretical calculations, evaluated by the competitive canonical unified statistical (CCUS) theory, below 300K in the LPL regime. The same trend was observed in the HPL regime below 350K, but the theoretical *k*(T) were higher than the experimental ones. Above 200K, the calculated rate coefficients are improved with respect to previous computational studies and are in excellent agreement with experimental literature data. In the LPL, the formation of CH_3NH becomes largely dominant below *ca*. 100K. Conversely, in the HPL regime, CH_2NH_2 is the only product below 100K, whereas CH_3NH becomes dominant at 298K with a branching ratio similar to the one found in the LPL regime (≈70%). At T>300 K, both reaction channels are competitive independently of the pressure regime.

[a] *Departamento de Química Física, Facultad de Ciencias y Tecnologías Químicas, Universidad de Castilla-La Mancha, Avda. Camilo José Cela 1b, 13071, Ciudad Real, Spain.*
[b] *Centro Singular de Investigación en Química Biológica y Materiales Moleculares (CIQUS), Campus Vida, Universidade de Santiago de Compostela, C/Jenaro de la Fuente s/n, 15782, Santiago de Compostela, Spain.*
[c] *Departamento de Química Física, Facultade de Química, Campus Vida, Universidade de Santiago de Compostela, Avda. das Ciencias s/n, 15782, Santiago de Compostela, Spain.*
[d] *CNRS, IPR (Institut de Physique de Rennes)-UMR 6251, Université de Rennes, F-35000 Rennes, France.*
[e] *Instituto de Investigación en Combustión y Contaminación Atmosférica (ICCA), Universidad de Castilla-La Mancha, Camino de Moledores s/n, 13071, Ciudad Real, Spain.*

† Footnotes relating to the title and/or authors should appear here.
Electronic Supplementary Information (ESI) available: [details of any supplementary information available should be included here]. See DOI: 10.1039/x0xx00000x

Introduction

In 1937, methylidyne (CH) radical became the first molecule ever detected in the interstellar medium (ISM).[1] Since then, with the development of the radioastronomy, more than 270 species have been detected in the ISM or circumstellar shells, where a wide temperature range is found (~10-1000 K). About one-third of these molecules are carbon-bearing species containing six atoms or more, defined as Complex Organic Molecules (hereafter COMs).[2] Among these observed COMs, the simplest amine (methylamine, CH_3NH_2) is considered a precursor of prebiotic molecules, such as amino acids like glycine (NH_2CH_2COOH). Although glycine has not yet been detected in the ISM,[3–5] it has been detected in several comets.[6,7] The depletion processes of CH_3NH_2 in the gas-phase must be known to be included in astrochemical models that simulates the chemistry of ISM. In particular, the gas-phase reaction with hydroxyl (OH) radicals, very abundant in the ISM and considered a key intermediate in many reactive interstellar processes,[8–11] is highly interesting, since their rate coefficient, k(T), has been observed to increase at the low temperatures of IS clouds with respect to k(298K).[12–16] Indeed, we have recently reported for the first time that k(22K) for the titled reaction increased about 20 times with respect to k(298K). OH radicals can be responsible of forming CH_2NH_2 (R1) or CH_3NH (R2) radicals from the H-abstraction from CH_3NH_2.

$$OH + CH_3NH_2 \rightarrow H_2O + CH_2NH_2 \quad (R1)$$
$$\rightarrow H_2O + CH_3NH \quad (R2)$$

Potential energy surfaces (PESs) calculations on the OH+CH_3NH_2 reaction found low energy barrier transition states for both H-abstraction channels (R1 and R2).[17–20] These findings are in agreement with a fast reaction, for which a k(298 K) of ~2×10^{-11} $cm^3molecule^{-1}s^{-1}$ has been reported. Experimental and theoretical branching ratios for this reaction have been also reported between 200-3000 K.[17,18,21] For example, the computed branching ratios at 298 K for channel R1 are 0.80,[17] 0.74[18] and 0.47,[21] respectively. Whereas, experimental studies show a yield of about 0.75 at 298 K for channel R1, demonstrating that the formation of CH_2NH_2 is the dominant product at room temperature.[19,22,23] To the best of our knowledge, branching ratios at T<200 K are not available until now.

Concerning the gas-phase reactivity of CH_3NH_2 towards OH radicals, it has already been studied up to 600 K (experimental) [21,22,24,25] and 3000 K (theoretical calculations).[18,21] Although a recent work investigated the kinetics of this reaction at 22 K, there are no experimental kinetic data between 22 K [26] and 295 K.[21,22,24,25] Between 22 and 3000 K, a smoking pipe-shape in the Arrhenius plot can be inferred, indicating a change in the reaction mechanism. The minimum k(T) is presently observed at around 550 K.[18] To have a better insight about the temperature evolution of the rate coefficient, we present in this work a combined experimental and theoretical study on the temperature dependence of k(T) in the 11.7-177.5 K and 10-1000 K ranges, respectively. The potential pressure dependence of k(T) was also experimentally investigated at several temperatures (50, 64, 77, 89 and 106 K), whereas calculations were carried out to obtain the temperature evolution of the low-pressure limit (LPL) and high-pressure limit (HPL) regimes. All previous theoretical works [17–21] employed the electronic structure calculations to obtain thermal rate coefficients at room temperature and above, except for the work of Onel *et al.*[21] that starts at 200 K. Therefore, this is the first study reporting theoretical thermal rate coefficients at lower temperatures than 200 K.

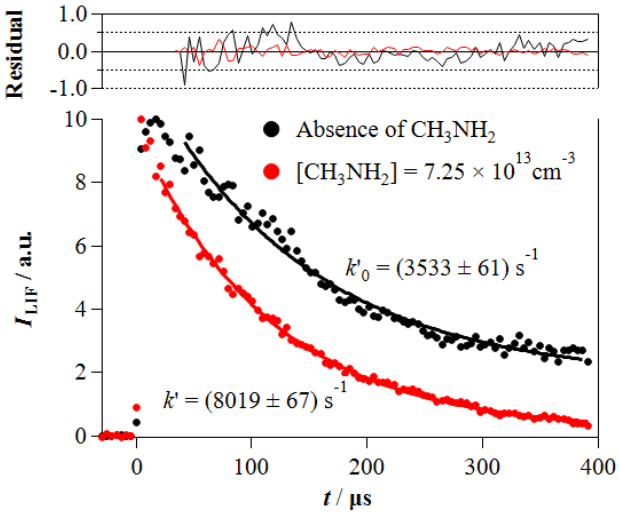

Fig. 1 Examples of the temporal profile of the LIF signal of OH radicals recorded in the absence and presence of CH_3NH_2 at 107.0 K.

Experimental Section

The low temperatures in the 11.7-177.5 K range are accessible using the pulsed CRESU (French acronym for *Reaction Kinetics in a Uniform Supersonic Flow*) system available in Ciudad Real (Spain). The pulsed laser photolysis (PLP) coupled to laser induced fluorescence (LIF) technique was employed to perform the kinetic study.

Pulsed CRESU apparatus

The CRESU apparatus and the experimental set-up have been described in detail in numerous previous works.[14–16,26–33] A set of seven Laval nozzles, after an appropriate aerodynamic characterization previously reported,[14–16,28,29,32–34] have been used to cover the 11.7-177.5 K temperature range. As shown in the Table S1 of the SI, all experiments, except for (64.2 ± 1.7) K, were performed using the pulsed mode, where the gas is pulsed at 10 Hz for T>11.7 K by means of a rotary disk with two symmetrical apertures. For experiments at 11.7 K, a rotary specific disk with only one aperture worked at 5 Hz. In this work, the He23K-HP Laval nozzle, providing a jet temperature of (51.6 ± 0.6) K,[30] in continuous mode, has been characterized using pulsed conditions to reduce the gas consumption. From impact pressure measurements, the resulting jet temperature was (49.9 ± 1.8) K with a reduction in the consumption

of gases of almost one order of magnitude with respect to the continuous mode.

Pulsed laser photolysis of gaseous H_2O_2 at *ca*. 248 nm was employed to generate OH radicals in the cold jet. The photolysis radiation is produced by a pulsed KrF excimer laser (Coherent, model ExciStar XS 200) and gaseous H_2O_2 was introduced in the *reservoir* inside the CRESU chamber by flowing a small portion of the buffer gas through a bubbler containing the pre-concentrated aqueous solution of H_2O_2. The produced OH radicals were excited at *ca*. 282 nm using a frequency-doubled dye laser (Lambda Physik, model ScanMate) pumped by a frequency-doubled Nd:YAG laser (Continuum, model Surelite). The temporal evolution of the subsequent LIF emission (I_{LIF}) from OH radicals was monitored at *ca*. 310 nm.

Determination of kinetic parameters

Under *pseudo*-first order conditions ($[CH_3NH_2]_0$>>$[OH]_0$), the temporal profile of I_{LIF} follows an exponential behaviour, as shown in the examples depicted in Figure 1. OH radicals are mainly lost by reaction with CH_3NH_2, but other loss processes such as reaction with H_2O_2 or diffusion out the detection zone, contribute to the observed decay of I_{LIF}. From the analysis of these decays after rotational relaxation previously explained,[14,28] the *pseudo*-first order rate coefficient, k', at a given $[CH_3NH_2]$ was obtained. k' is always measured in the absence of CH_3NH_2, i.e., k'_0. As shown in Fig. 2, k'-k'_0 values are linearly dependent on $[CH_3NH_2]$ in a certain range of concentrations. Hence, varying $[CH_3NH_2]$ allows to obtain individual k(T) from the slope of k'-k'_0 *versus* $[CH_3NH_2]$ plots as described elsewhere.[14,15,33,16,26–32] However, at high $[CH_3NH_2]$, these plots exhibit a downward curvature (see Fig. S4 of the Supplementary Information), which could be attributed to the formation of methylamine dimers, $(CH_3NH_2)_2$, especially at very low temperatures. For that reason, the concentration range where the linearity is maintained is drastically reduced at 11.7 with respect to 177.5 K (see Fig. 2). This curvature is mostly usual in the CRESU experiments; hence, it is of great importance to keep the $[CH_3NH_2]$ low enough in order to not underestimate k(T) at each temperature.

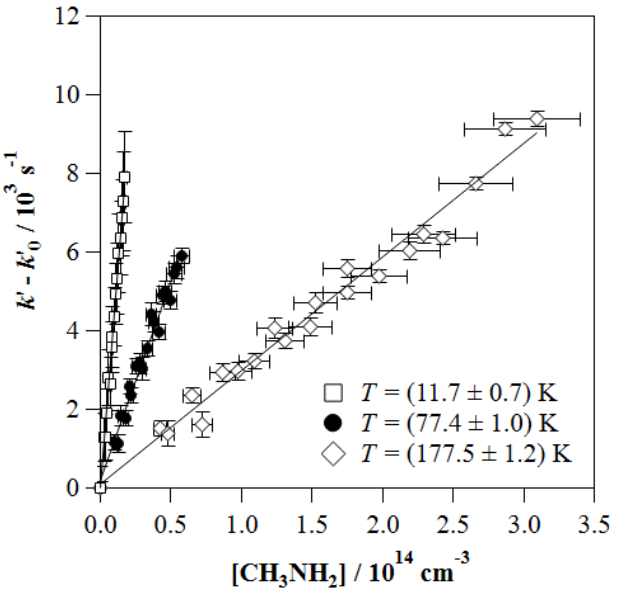

Fig. 2. Examples of k'-k'_0 vs $[CH_3NH_2]$ plots at different temperatures. Uncertainties in $[CH_3NH_2]$ are conservatively considered as ±10% and in k'-k'0 are the standard deviation obtained from the fit of the LIF OH decays.

To obtain reliable values of k(T), it is also essential to accurately know $[CH_3NH_2]$ in the jet. It was calculated from the total gas density in the jet (n_{jet}), considering the mass flow rate ($F_{CH_3NH_2/buffer}$) introduced in the nozzle reservoir of a diluted CH_3NH_2 mixture stored in a 20-L or 50-L bulb (dilution factor, $f_{CH_3NH_2}$ =$P_{CH_3NH_2}$/P_{Total} in the bulb), and the total mass flow rate (F_{total}) through the reservoir.

$$[CH_3NH_2] = \frac{F_{CH_3NH_2/buffer}}{F_{total}} n_{jet} f_{CH_3NH_2} \quad (1)$$

Buffer gases are mainly He, N_2, Ar or binary mixtures of Ar-N_2 or He-N_2 (see Table S1 of the Supplementary Information). F_{total} is the sum of the main mass flow of buffer gas (F_{buffer}), the mass flow of the buffer gas through the bubbler with H_2O_2 ($F_{H_2O_2}$) and $F_{CH_3NH_2/buffer}$. The ranges of these experimental parameters for all investigated temperatures are listed in Table S1. All gas flows were controlled by mass flow controllers which were periodically calibrated for the buffer gas used (Sierra Instruments Inc., models Smart-Trak 2 and 100 and MicroTrak 101).

$f_{CH_3NH_2}$ was regularly checked offline by UV absorption spectroscopy between 189 and 260 nm, as explained in the SI and in Ref. [16,27]. UV spectra of several samples of the diluted CH_3NH_2 mixture from the storage bulb were recorded at room temperature A maximum difference of 7% was found between the UV and partial pressure measurements of $f_{CH_3NH_2}$, but typically this difference was lesser than 2%.

Chemicals

Gases: He, N_2 and Ar (99.999%, Nippon Gases Europe) and CH_3NH_2 (>99.0%, Merck and 99.5%, Nippon Gases Spain) were used as supplied. An aqueous solution of hydrogen peroxide (Sharlab, initially at 50% w/w) was preconcentrated as described earlier.[35] After use, the H_2O_2 bubbler was stored in a refrigerator at 4°C to prevent from thermal decomposition.

Theoretical Section

Electronic structure calculations

All electronic structure calculations were performed at the M08HX [36] Density Functional Theory (DFT) level with the MG3S basis set.[37] This DFT method was previously applied to the methyl hydrogen abstraction reaction from methanol by the hydroxyl radical with good results.[38] To check the adequacy of the method for reactions R1 and R2, we have benchmarked the DFT results against single-point calculations performed at the RI-CCSD(T)-F12 level with the cc-pVTZ-F12 basis set over the M08HX optimized geometries. The relative energies obtained by the two methods are listed in Table 1. The results show that the M08HX method provides similar barrier heights when compared to the CCSD(T) single-point calculations.

Unfortunately, even though most of the previous works used single point CCSD(T) calculations as benchmark, the comparison shows mixed results. Probably the reason for this disparity is the difference in the optimized geometries, which were obtained using diverse electronic structure levels. For instance, Tian *et al.*[18] reported CCSD/6-31G(d) geometry optimizations obtaining very tight transition states with imaginary frequencies of 1388*i* and 1926*i* cm^{-1} for TS1 and TS2, respectively, in which the former transition state is clearly favored. Onel *et al.*[21] at the MP2/aTZ level, obtained three transition states for the hydrogen abstraction from the methyl group and only one for the abstraction of the amine group, being the lowest energy transition state of R1 isoenergetic with TS2. Borduas *et al.*[20] employing M06-2X/6-31G(2df,p) reported an energy profile like ours (see our Figure 3 and Scheme 1 of Ref. 20) but with a destabilized C1 pre-reactive complex. In this work, we have obtained two pre-reactive complexes when following the minimum energy path (MEP) from TS1 (leading to C1) and TS2a and TS2b (leading to C2). The main difference between TS2a and TS2b is in the CN…OH dihedral angles which are 117 (TS2a) and 22 degrees (TS2b), respectively. For the three transition states, the MEP was obtained by employing the Page-McIver algorithm [39] with a stepsize of 0.005 Bohr (in mass-scaled coordinates) and Hessian calculations every 10 steps. All frequencies were scaled by the recommended factor of 0.973.[40] The DFT and CCSD(T) electronic structure calculations were performed with Gaussian16 [41] and Orca,[42] respectively. All dynamics calculations were carried out with Pilgrim.[43]

Thermal rate coefficients

As shown in Figure 3, the hydrogen abstraction reaction from methylamine by the hydroxyl radical takes place in two steps. The first step is an association reaction that may lead to different pre-reactive hydrogen bonded complexes, whereas the second step is the hydrogen abstraction reaction. There are also post-reaction complexes, but they do not have any effect on the dynamics so were not further pursued in this study. For the evaluation of the rate coefficients at the low-pressure limit (LPL) and the high-pressure limit (HPL), we applied the competitive canonical unified theory (CCUS). In this methodology, the rate coefficient for each channel, k_j^{CCUS}, is given by:[38]

$$k_j^{\mathrm{CCUS}} = \frac{k_a}{k_a + k_{\mathrm{H},1} + k_{\mathrm{H},2}} k_{\mathrm{H},j} \qquad (2)$$

where k_a and $k_{\mathrm{H},j}$ are the association and hydrogen abstraction (j =1, 2) rate coefficients, respectively. The association rate coefficient was calculated by applying the expression proposed by Georgievskii and Klippenstein for dipole-dipole interactions.[44] It is given by:

$$k_a = C\mu^{-1/2}(d_{\mathrm{CH_3NH_2}} d_{\mathrm{OH}})^{2/3} T^{-1/6} \qquad (3)$$

where μ is the reduced mass of the two fragments (in amu), T is the temperature (in K) and $d_{\mathrm{CH_3NH_2}} = 1.31$ D and $d_{\mathrm{OH}} = 1.66$ D are the dipole moments of methylamine and the OH radical, respectively, obtained at the M08HX level. The parameter C = 1.83×10^{-9} has the units that convert Eq. (3) to $cm^3 molecule^{-1} s^{-1}$.

Canonical variational transition state theory with the small-curvature tunneling approximation (CVT/SCT) [45] was employed to evaluate the hydrogen abstraction rate coefficients. For reaction R1, the rate coefficient expression can be written as:

$$k_{\mathrm{H},1}^{\mathrm{CVT/SCT}} = \sigma_1 \Gamma_1^{\mathrm{CVT}} \kappa_{E_{0,1}}^{\mathrm{CVT/SCT}} k_1^{\mathrm{TST}} \qquad (4)$$

where $\sigma_1$is the symmetry number and accounts for the degeneracy of the reaction path,[46] which in this case is two because there are two equivalent TS1 structures with C_1 symmetry, Γ_1^{CVT} is the variational coefficient that corrects the conventional transition state theory rate coefficients k_1^{TST} (for the passage of reactants through TS1).

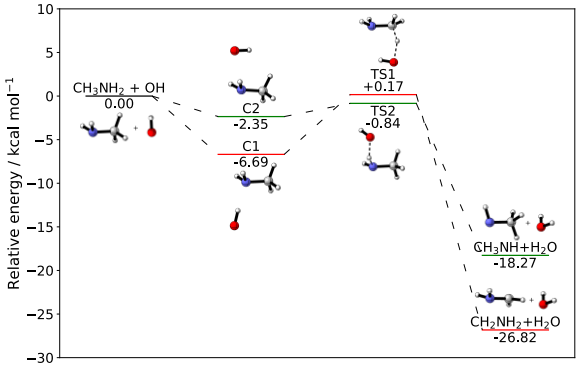

Fig. 3. Reaction profile for the H-abstraction reaction of CH_3NH_2 by the OH radical through channels R1 (red) and R2 (green). The relative energies refer to the M08HX/MG3S values of Table 1 plus the difference in zero-point energies (ZPEs) with respect to reactants. Transition state TS2b (not plotted) differs slightly in energy from TS2a.

Table 1. Relative energies, (in kcal/mol) of the stationary points at the optimized M08HX/MG3S level, ΔE_{DFT}, and single-point RI-CCSD(T)-F12 /cc-pVTZ-F12 calculations over the M08HX geometries (ΔE_{CC}). For comparison, relative energies including the zero-point energies are also listed.

Energy / species	ΔE_{DFT}	ΔE_{CC}	Δ(E+ZPE)			
CH_3NH_2 + OH	0.00	0.00	0.00[a]	0.00[b]	0.00[c]	0.00[d]
C1	-8.86	-8.70	-6.69	-8.46	-6.4	-5.4
C2	-3.57	-2.29	-2.35	-0.61	---	-0.2
TS1	0.85	1.08	0.17	-0.52	-2.0	1.2
TS2a	-0.50	-0.57	-0.84	1.02	-2.0	0.2
TS2b	-0.41	-0.53	-0.77	---	---	---
CH_2NH_2 + H_2O	-26.22	-25.15	-26.82	-23.19	-26.5	-26.0
CH_3NH + H_2O	-16.93	-17.87	-18.27	-17.09	-19.6	-19.0

[a]This work, M08HX/MG3S level.
[b]Tian *et al.*[18], CCSD(T)/6-311+G(2d,2p)//CCSD/6-31G(d).
[c]Onel *et al.*[21], CCSD(T*)-F12a/aTZ//MP2/aTZ level.
[d]Borduas *et al.*[20], G3X-K//M06-2X/6-31G(2df, p) level.

The variational coefficient minimizes the recrossing along the minimum energy path (MEP), that is, it considers that the bottleneck for reaction is located at the highest value of the Gibbs free energy along the path. Therefore, $0 < \Gamma_1^{\mathrm{CVT}} \leq 1$, being the unity when the maximum of the free energy is located at the transition state. Additionally, CVT/SCT incorporates quantum effects through the tunneling transmission coefficient $\kappa_{E_{0,1}}^{\mathrm{CVT/SCT}}$, which depends on the pressure limit because E_0 represents the lowest temperature at which the system can tunnel.

The pre-reactive complex is unreachable in the LPL because the reactants cannot be stabilized by collisions, and the lowest energy at which tunneling can occur is the sum of the ground-state energies of the two reactants, $E_{0,1} = E_0(\mathrm{R})$, where R means reactants. In the HPL, the collisions with a third body can fully stabilize the pre-reactive complexes and tunneling can occur from the ground-state energies of these complexes, i.e., $E_{0,1} = E_0(\mathrm{C1})$, where $E_0(\mathrm{C1})$ is the ground-state energy of C1.[47]

Reaction R2 presents two transition states, TS2a and TS2b and the MEPs lead to the same pre-reactive complex, C2. In this case:

$$k_{\mathrm{H},2}^{\mathrm{CVT/SCT}} = \sigma_2 \left(\Gamma_{2\mathrm{a}}^{\mathrm{CVT}} \kappa_{E_{0,2\mathrm{a}}}^{\mathrm{CVT/SCT}} k_{2\mathrm{a}}^{\mathrm{TST}} + \Gamma_{2\mathrm{b}}^{\mathrm{CVT}} \kappa_{E_{0,2\mathrm{b}}}^{\mathrm{CVT/SCT}} k_{2\mathrm{b}}^{\mathrm{TST}} \right) \quad (5)$$

where $\sigma_2 = 2$ and $k_{2\mathrm{a}}^{\mathrm{TST}}$ and $k_{2\mathrm{b}}^{\mathrm{TST}}$ are the TST rate coefficients for the passage of reactants through TS2a and TS2b, respectively. Notice that $E_{0,2\mathrm{a}} = E_{0,2\mathrm{b}} = E_0(\mathrm{R})$ in the LPL and that $E_{0,2\mathrm{a}} = E_{0,2\mathrm{b}} = E_0(\mathrm{C2})$ in the HPL. For the latter, the difference in energy between CCSD(T) and M08HX at C2 is of 1.28 kcal/mol, so the lowest tunneling energy calculated at the DFT level incorporated this difference in the evaluation of the tunneling transmission coefficient.

We have also incorporated torsional anharmonicity on the motion of the OH about the methyl and amine groups in the transition state structures. The one-dimensional partition function associated with each of the torsions was calculated as a direct sum of the energy levels, which were obtained by fitting the potential to a Fourier series and solving the resulting Schrödinger equation (see Figure 4).[48,49] The torsional anharmonic partition function replaces the torsional harmonic-oscillator partition function in the TST rate coefficient of Eq. (5). Specifically, the normal mode identified with the torsion, ω_τ, with a quantum harmonic-oscillator partition function given by

$$q_\tau = \frac{e^{-\beta\hbar\omega_\tau/2}}{1-e^{-\beta\hbar\omega_\tau}} \quad (6)$$

is replaced by the torsional anharmonic partition function

$$q_\tau = \sum_i e^{-\beta E_{\tau,i}} \quad (7)$$

where $E_{\tau,i}$ is the energy of the i^{th} level, $\hbar$ is Planck's constant divided by 2π, $\beta = (k_B T)^{-1}$ where k_B is Boltzmann's constant. The torsional frequency, ω_τ, is 371 cm^{-1} for TS1 and 99 and 145 cm^{-1} for TS2a and TS2b, respectively.

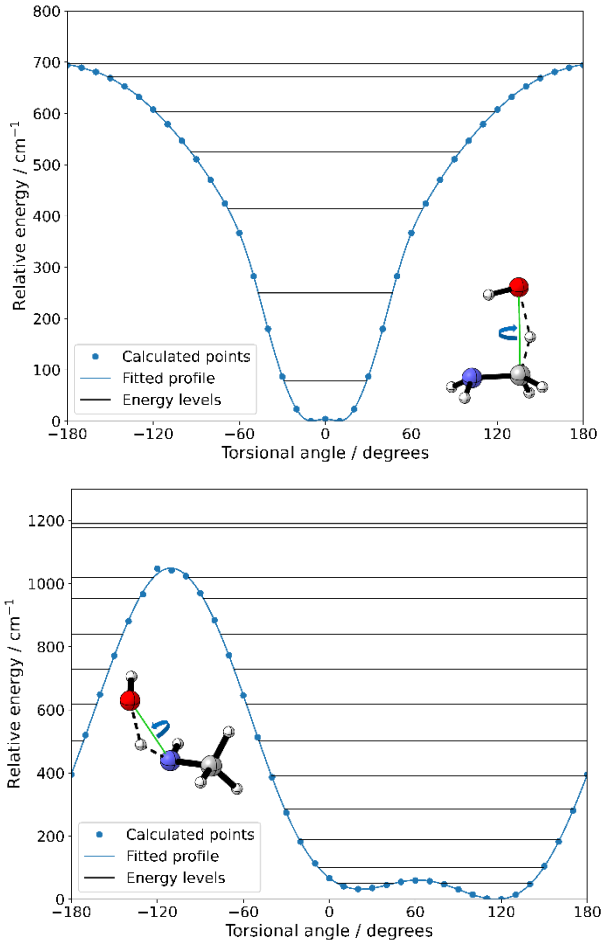

Fig. 4. The calculated potential at the M08HX/MG3S level (dots) and the fitted Fourier series potential (blue line) are plotted to represent the torsional potential about the C…O (left) and N…O (right) atoms. The horizontal lines correspond to the energy levels.

Results and discussion

Experimental pressure and temperature dependence of *k*(T)

The possible pressure (or gas density) dependence of k(T) was experimentally investigated at around 50, 64, 76, 89, and 106 K. Figure 5 shows two examples of k(T) at 50 and 106 K as a function of total pressures, corresponding to total gas densities between 1.50×10^{16} and 19.5×10^{16} cm^{-3}. As shown, there is no pressure dependence of k(T) within the gas density range investigated and accessible with the present experimental set-up. These results are in excellent agreement with those from González *et al.*[26] who did not observe any pressure dependence of k(22 K). Thus, in Table 2 we report k(T) obtained by combining all measured k'-k'_0, as presented in Figure 2. These k(T) are plotted in Figure 6 (black circles) along with the k(22 K) previously reported (red circle).[26] The total uncertainties in k(T) shown in the Figure 6 and in the Table 2 include the statistical errors (±2σ) derived from the slope of the k'-k'_0 versus [CH_3NH_2] and the systematic errors, which has been previously estimated to be no more than 10% of the measured k(T).[14,15,32,33] The total uncertainty in k(T) has been calculated as the square root of the sum of the ±2σ

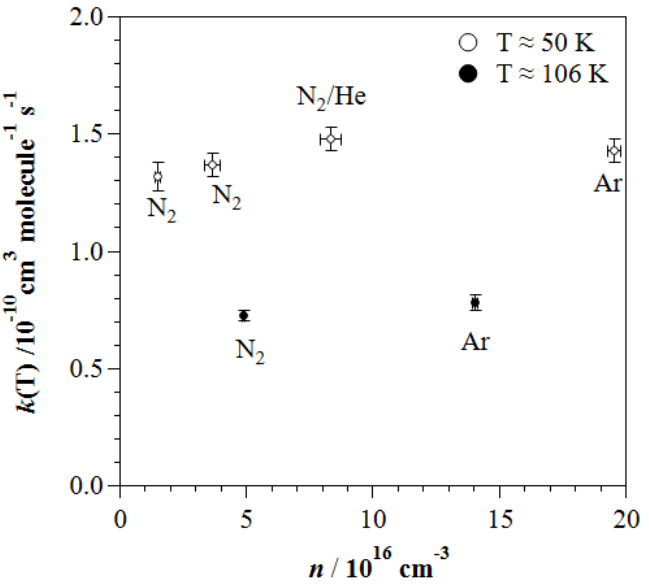

Fig. 5. Dependence of k(T) at ca. 50 and 106 K as a function of the gas density. The bath gas is indicated next to each point. Error bars in k(T) and n represent ±σ uncertainty.

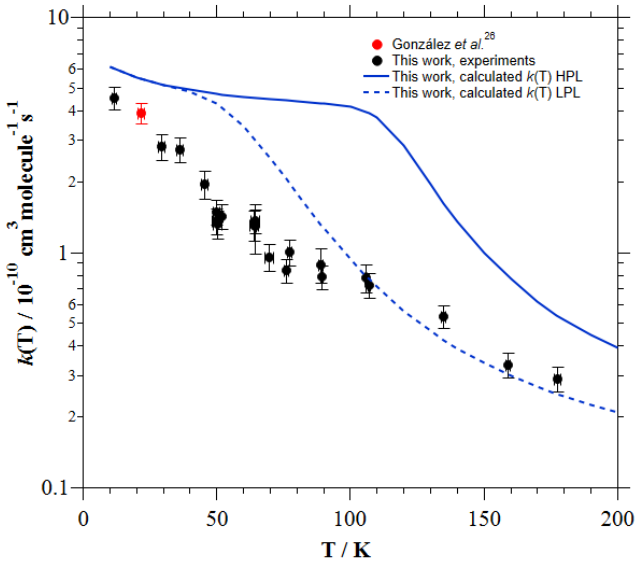

Fig. 6. Temperature dependence of k(T) obtained in this work from experimental measurements and theoretical calculations and comparison with the previous data from González *et al*.[26]

statistical error and the systematic error squared. As it can be seen, k(T) is continuously increasing while lowering the gas temperature from 177.5 K to 11.7 K. The published k(T) at 22 K[26] agrees with the observed trend in k(T). However, although the observed increase of k(T) is remarkable (more than one order of magnitude from k(177.5 K) to k(11.7 K)), it seems to slow down at T<22 K. This levelling out of k(T) has been already observed more clearly in some other OH-reactions studied in our research group.[15,16] This effect may occur because the rate coefficient approaches the capture limit (see next section). The calculated HPL and LPL of k(T) are also presented in Figure 7. In this figure, the plot shows a complete picture of k(T) *versus* T between 0 and 1000 K that compares the results presented here with those of previous studies (available at T>295 K). The k(T) of the title reaction was studied previously over the whole 295-3000 K temperature range, including experiment and theory. Regarding the experimental temperature dependence of k(T), a non-Arrhenius behavior in the temperature range studied (295-600 K) was observed, increasing the k(T) at the lowest temperatures. This change in the trend on the temperature dependence of k(T) has been already observed at low temperatures for other OH-reactions, see *e.g.*, OH+CH_3OH or OH+CH_3CHO.[15,16]

Table 1 Experimental rate coefficients $k(T)$ (±2σ statistical and 10% systematic errors) as a function of temperature.

~T/K	T/K	n / 10^{16} cm^{-3}	[CH_3NH_2] / 10^{13} cm^{-3}	k(T) / 10^{-11} cm^3 molec^{-1} s
12	11.7 ± 0.7	6.88 ± 0.62	0.3 – 1.7	45.5 ± 5.0
30	29.2 ± 1.1	8.68 ± 0.53	0.6 – 2.6	28.1 ± 3.5
	36.2 ± 1.2	17.7 ± 0.9	0.3 – 2.5	27.4 ± 3.2
	45.3 ± 1.3	4.23 ± 0.28	0.4 – 2.7	19.6 ± 2.7
50	49.9 ± 1.4	8.33 ± 0.41	0.5 – 5.8	14.8 ± 1.8
	49.9 ± 1.8	3.67 ± 0.32	0.5 – 3.0	13.7 ± 1.7
	50.5 ± 1.6	1.50 ± 0.12	0.8 – 5.2	13.4 ± 1.9
	52.1 ± 0.5	19.5 ± 0.3	0.4 – 1.9	14.3 ± 1.8
64	64.1 ± 1.6	4.63 ± 0.27	0.5 – 2.7	13.1 ± 1.9
	64.2 ± 1.7	2.24 ± 0.15	0.9 – 5.2	13.7 ± 1.6
	64.4 ± 0.6	17.36 ± 0.29	0.9 – 2.3	13.0 ± 3.1
	69.5 ± 1.6	3.26 ± 0.19	2.4 – 5.2	9.56 ± 1.23
	76.0 ± 0.8	15.0 ± 0.3	0.3 – 2.4	8.37 ± 0.97
	77.4 ± 1.0	2.38 ± 0.08	1.0 – 5.8	10.1 ± 1.3
89	89.1 ± 0.7	43.3 ± 0.5	0.9 – 3.5	8.89 ± 1.47
	89.5 ± 0.6	18.2 ± 0.3	1.1 – 8.5	7.91 ± 0.91
106	106.0 ± 0.6	14.0 ± 0.1	0.7 – 5.0	7.79 ± 1.06
	107.0 ± 0.5	4.90 ± 0.06	0.7 – 6.1	7.28 ± 0.86
	135.0 ± 0.8	29.4 ± 0.5	2.6 – 16	5.36 ± 0.61
	158.8 ± 0.6	7.40 ± 0.07	3.3 – 23	3.44 ± 0.44
	177.5 ± 1.2	6.71 ± 0.11	4.3 – 31	2.89 ± 0.35

Computed pressure and temperature dependence of k(T)

As shown in Figure 7, the theoretical calculations show that the LPL and HPL rate coefficients converge at temperatures below 40 K and at temperatures above 500 K. The largest difference between the

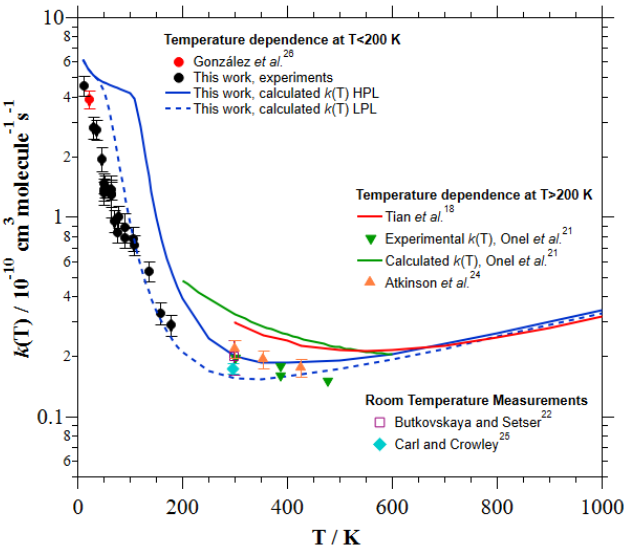

Fig. 7. Temperature dependence of k(T) for the title reaction between 10 and 1000 K.

two limits occurs at about 100 K that reaches a factor of five. However, at 200 K the difference between the two regimes is just about a factor of two.

This difference is not as substantial as in the methanol+OH reaction, because the barrier heights for the hydrogen abstractions from the CH_3 and OH groups from methanol are above the ground-state energy of reactants, and at very low temperatures tunneling cannot significantly accelerate the reaction process in the LP regime. By contrast, in the present work, for the H-abstraction from the NH_2 group, whose transition state is below reactants, the rate coefficient increases with decreasing temperature.

Notice that reactions R1 and R2 present two reaction bottlenecks, the first involves a barrierless reaction and corresponds to the association of the two molecules. The association rate coefficient is larger at the lowest temperature, $k_a(10\ \mathrm{K}) = 6.19 \times 10^{-10}$ cm^3 molecule^{-1} s^{-1}, and it slightly decreases when increasing temperature as a function of $T^{-1/6}$. The second reaction bottleneck is associated with the transition states resulting from the hydrogen abstraction reactions. In the LPL at very low temperatures, if the two barriers were slightly above the ground-state energy of reactants, $k_a \gg k_{\mathrm{H}}$ and therefore,

$$k_j^{\mathrm{CCUS}} \approx k_{\mathrm{H},j} \qquad (8)$$

This situation occurs in the CH_3OH + OH reaction, as mentioned above. However, if there are transition states lying below reactants (TS2a and TS2b), $k_{\mathrm{H},2} \gg k_a \gg k_{\mathrm{H},1}$, and the total rate coefficient is limited by the association reaction, i.e.,

$$k^{\mathrm{CCUS}} \approx k_2^{\mathrm{CCUS}} \approx k_a \qquad (9)$$

In the HPL, at very low temperatures $k_{\mathrm{H},1} \gg k_a \gg k_{\mathrm{H},2}$ because the contribution from tunneling to the hydrogen abstraction reaction from the methyl group is large

$$k^{\mathrm{CCUS}} \approx k_1^{\mathrm{CCUS}} \approx k_a \qquad (10)$$

With increasing temperature, the association reaction becomes larger than the abstraction (above 50 K in the LPL and above 100 K in the HPL) and the only difference between both pressure regimes is the tunneling contribution, which is more relevant in the high-pressure limit. Above 500 K the tunneling contribution becomes negligible, and both pressure limits converge with a monotonic increase of the rate coefficients.

Additionally, torsional anharmonicity also plays a relevant role and increases the rate coefficients with respect to the harmonic oscillator ones in the whole temperature range between 10 and 1000 K. Its influence is greater at low temperatures and more important for R1 than for R2. Specifically, at T = 100 K, it contributes to channels R1 and R2 with factors of 5.1 and 1.5, respectively. These factors decrease to 2.9 (R1) and 1.4 (R2) at T = 300 K. At higher temperatures, the factors remain close to the ones at room temperature, being 3.1 (R1) and 1.2 (R2) at T = 1000 K.

The calculated rate coefficients reach a minimum at about 300 K in the LPL and at about 400 K in the HPL. This feature is typical of hydrogen abstraction bimolecular reactions with very stable pre-reactive complexes and low-lying transition states due to the influence of two opposing factors. On the one hand, quantum effects (penetration through the potential barrier) decrease with increasing temperature, but on the other hand the classical passage over the barrier is favored by high temperatures. The valley is attained when the cancellation of these two factors is maximum, and it is well reproduced by the calculated CCUS rate coefficients.

Once rate coefficients were obtained for each exit channel using eq. 4 and 5, the branching ratios leading to the formation of CH_2NH_2 (R1) or CH_3NH (R2) could be determined for every temperature investigated theoretically. Results are shown in Table S10 of the supplementary information and the temperature evolution of these branching ratios has been plotted in Figure 8 for the two pressure regimes. Interestingly, there is a significant temperature dependence of these branching ratios which is of major importance when importing this class of data in a chemical network such as those used to evaluate de chemical evolution of interstellar clouds. In the LPL conditions, the channel leading to CH_3NH becomes largely dominant below room temperature and is unique below ca. 100 K.

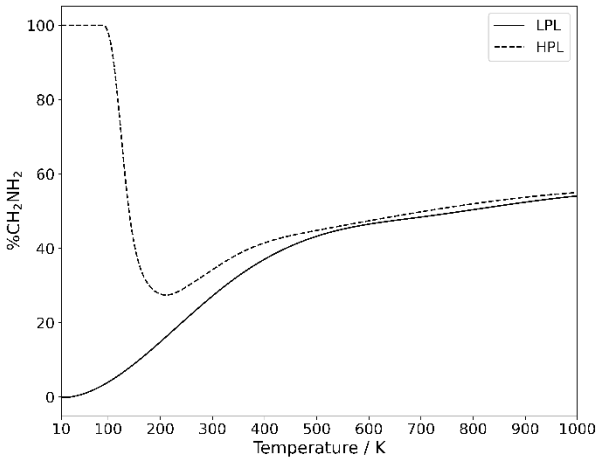

Fig. 8. Temperature dependence of the branching ratio for CH_2NH_2 radical between 10 and 1000 K.

Conversely, in the HPL regime, CH_2NH_2 is the only available channel below 100 K whereas CH_3NH becomes dominant at room temperature with a branching ratio close to the one found in the LPL regime. At the highest temperatures, both possible channels are of the same importance independently of the pressure regime. Then at the lowest temperatures, the reaction switches from a 100% CH_3NH formation in the LPL regime to a 100% CH_2NH_2 production in the HPL conditions. At room temperature, our results are in qualitative agreement with the theoretical results of Onel *et al.* that slightly favor the CH_3NH formation. The experimental results favor the R1 channel by approximately a factor of three. It should be noticed that

the branching ratios are very sensitive to the calculated barrier heights. Thus, an increment of the R2 barrier by 0.5 kcal/mol and a diminishment of the R1 barrier by the same factor reproduces the experimental branching ratio at room temperature, whereas the total rate coefficient continued to be very similar. However, even after these changes the branching ratios at the lowest temperatures remained unaltered, which give us some confidence about the products distribution in the interstellar media.

Conclusions

In this work, the rate coefficients for the $OH+CH_3NH_2$ reaction have been experimentally and theoretically determined in a wide temperature range (10-1000 K). The observed increase of k(T) with decreasing temperature below room temperature is concluded to be a consequence of the quantum mechanical tunneling. Conversely, at T>500 K the tunneling effect is negligible, observing an increase of k(T) with increasing temperature. The computed k(T) around 300-500 K are in excellent agreement with those reported experimentally, while Tian *et al*.[18] and Onel *et al*.[21] overestimate k(T) in that T-range. Above 600 K, our computational study perfectly agrees with the previous study from Tian *et al*.[18] According to the calculations, the experimental k(T) fall very close to the low pressure limit. This implies that the experimental results obtained here are applicable to the temperatures and pressures of the interstellar medium. In this environment, LPL prevails since the gas densities are extremely low. Our calculations also suggest that the $OH+CH_3NH_2$ reaction only forms CH_3NH radicals in the interstellar conditions of molecular clouds and pre-stellar cores.

Author Contributions

D.G and S.E. performed the experiments and data analysis and wrote the original draft of the paper; ALS, EMN, and AFR carried out the theoretical calculations; AC and BB reviewed the draft; E.J. designed and supervised the experiments as well as got funds for carrying out the present experimental research; All authors contributed to the critical review and edition of the paper.

Conflicts of interest

There are no conflicts to declare.

Acknowledgements

This work has been supported by the Spanish Ministry of Science and Innovation (MICINN) through the CHEMLIFE project (Ref.: PID2020-113936GB-I00), the regional government of Castilla-La Mancha through CINEMOL project (Ref.: SBPLY/19/180501/000052) and by the University of Castilla-La Mancha – UCLM (*Ayudas para la financiación de actividades de investigación dirigidas a grupos* (REF: 2019-GRIN-27175). DG and SE also acknowledge UCLM (*Plan Propio de Investigación*) and CINEMOL project, respectively, for funding their contracts during the performance of this investigation. This work was partially supported by the Consellería de Cultura, Educación e Ordenación Universitaria (Centro singular de investigación de Galicia acreditación 2019-2022, ED431G 2019/03 and Grupo de referencia competitiva ED431C 2021/40) and the European Regional Development Fund (ERDF), and the Ministerio de Ciencia e Innovación through Grant #PID2019-107307RB-I00. ALS thanks Xunta de Galicia for financial support through a postdoctoral grant. AFR, EMN and ALS thank the Centro de Supercomputación de Galicia (CESGA) for the use of their computational facilities.

Notes and references

1 P. Swings and L. Rosenfeld, *Astrophys. J.*, 1937, **86**, 483.
2 E. Herbst and E. F. van Dishoeck, *Annu. Rev. Astron. Astrophys.*, 2009, **47**, 427–480.
3 P. D. Holtom, C. J. Bennett, Y. Osamura, N. J. Mason and R. I. Kaiser, *Astrophys. J.*, 2005, **626**, 940–952.
4 J.-B. Bossa, F. Duvernay, P. Theulé, F. Borget, L. D'Hendecourt and T. Chiavassa, *Astron. Astrophys.*, 2009, **506**, 601–608.
5 C.-W. Lee, J.-K. Kim, E.-S. Moon, Y. C. Minh and H. Kang, *Astrophys. J.*, 2009, **697**, 428–435.
6 K. Altwegg, H. Balsiger, A. Bar-Nun, J. J. Berthelier, A. Bieler, P. Bochsler, C. Briois, U. Calmonte, M. R. Combi, H. Cottin, J. De Keyser, F. Dhooghe, B. Fiethe, S. A. Fuselier, S. Gasc, T. I. Gombosi, K. C. Hansen, M. Haessig, A. Jäckel, E. Kopp, A. Korth, L. Le Roy, U. Mall, B. Marty, O. Mousis, T. Owen, H. Rème, M. Rubin, T. Sémon, C. Y. Tzou, J. H. Waite and P. Wurz, *Sci. Adv.*, 2016, **2**, 1–6.
7 J. E. Elsila, D. P. Glavin and J. P. Dworkin, *Meteorit. Planet. Sci.*, 2009, **44**, 1323–1330.
8 K. Acharyya, E. Herbst, R. L. Caravan, R. J. Shannon, M. A. Blitz and D. E. Heard, *Astron. Astrophys*, 2015, **113**, 2243–2254.
9 S. Cazaux, V. Cobut, M. Marseille, M. Spaans and P. Caselli, *Astron. Astrophys.*, , DOI:10.1051/0004-6361/201014026.
10 J. R. Goicoechea, C. Joblin, A. Contursi, O. Berné, J. Cernicharo, M. Gerin, J. Le Bourlot, E. A. Bergin, T. A. Bell and M. Röllig, *Astron. Astrophys.*, 2011, **530**, L16.
11 H. Linnartz, S. Ioppolo and G. Fedoseev, *Int. Rev. Phys. Chem.*, 2015, **34**, 205–237.
12 A. Potapov, A. Canosa, E. Jiménez and B. Rowe, *Angew. Chemie Int. Ed.*, 2017, **56**, 8618–8640.
13 D. E. Heard, *Acc. Chem. Res.*, 2018, **51**, 2620–2627.
14 A. J. Ocaña, S. Blázquez, B. Ballesteros, A. Canosa, M. Antiñolo, J. Albaladejo and E. Jiménez, *Phys. Chem. Chem. Phys.*, 2018, **20**, 5865–5873.
15 A. J. Ocaña, S. Blázquez, A. Potapov, B. Ballesteros, A. Canosa, M. Antiñolo, L. Vereecken, J. Albaladejo and E. Jiménez, *Phys. Chem. Chem. Phys.*, 2019, **21**, 6942–6957.
16 S. Blázquez, D. González, E. M. Neeman, B. Ballesteros, M. Agúndez, A. Canosa, J. Albaladejo, J. Cernicharo and E. Jiménez, *Phys. Chem. Chem. Phys.*, 2020, **22**, 20562–20572.
17 A. Galano and J. R. Alvarez-Idaboy, *J. Chem. Theory*

Comput., 2008, **4**, 322–327.
18 W. Tian, W. Wang, Y. Zhang and W. Wang, *Int. J. Quantum Chem.*, 2009, **109**, 1566–1575.
19 L. Onel, M. Blitz, M. Dryden, L. Thonger and P. Seakins, *Environ. Sci. Technol.*, 2014, **48**, 9935–9942.
20 N. Borduas, J. P. D. Abbatt, J. G. Murphy, S. So and G. Da Silva, *Environ. Sci. Technol.*, 2016, **50**, 11723–11734.
21 L. Onel, L. Thonger, M. A. Blitz, P. W. Seakins, A. J. C. Bunkan, M. Solimannejad and C. J. Nielsen, *J. Phys. Chem. A*, 2013, **117**, 10736–10745.
22 N. I. Butkovskaya and D. W. Setser, *J. Phys. Chem. A*, 2016, **120**, 6698–6711.
23 C. J. Nielsen, B. D'Anna, M. Karl, M. Aursnes, A. Boreave, R. Bossi, A. J. Coldevin Bunkan, M. Glasius, M. Hallquist, A.-M. Kaldal Hansen, K. Kristensen, T. Mikoviny, M. M. Maguta, M. Müller, Q. Nguyen, J. Westerlund, K. Salo, H. Skov, Y. Stenstrøm and A. Wisthaler, *NILU*, 2011, **2**, University of Oslo.
24 R. Atkinson, R. A. Perry and J. N. Pitts, *J. Chem. Phys.*, 1977, **66**, 1578–1581.
25 S. A. Carl and J. N. Crowley, *J. Phys. Chem. A*, 1998, **102**, 8131–8141.
26 D. González, B. Ballesteros, A. Canosa, J. Albaladejo and E. Jiménez, *Front. Astron. Sp. Sci.*, 2022, **8**, 1–11.
27 E. M. Neeman, D. González, S. Blázquez, B. Ballesteros, A. Canosa, M. Antiñolo, L. Vereecken, J. Albaladejo and E. Jiménez, *J. Chem. Phys.*, 2021, **155**, 034306.
28 E. Jiménez, B. Ballesteros, A. Canosa, T. M. Townsend, F. J. Maigler, V. Napal, B. R. Rowe and J. Albaladejo, *Rev. Sci. Instrum.*, 2015, **86**, 45108.
29 A. Canosa, A. J. Ocaña, M. Antiñolo, B. Ballesteros, E. Jiménez and J. Albaladejo, *Exp. Fluids*, 2016, **57**, 1–14.
30 E. Jiménez, M. Antiñolo, B. Ballesteros, A. Canosa and J. Albaladejo, *Phys. Chem. Chem. Phys.*, 2016, **18**, 2183–2191.
31 M. Antiñolo, M. Agundez, E. Jimenez, B. Ballesteros, A. Canosa, G. El Dib, J. Albaladejo and J. Cernicharo, *Astrophys. J.*, 2016, **823**, 25.
32 A. J. Ocaña, E. Jiménez, B. Ballesteros, A. Canosa, M. Antiñolo, J. Albaladejo, M. Agúndez, J. Cernicharo, A. Zanchet, P. del Mazo, O. Roncero and A. Aguado, *Astrophys. J.*, 2017, **850**, 28.
33 S. Blázquez, D. González, A. García-Sáez, M. Antiñolo, A. Bergeat, F. Caralp, R. Mereau, A. Canosa, B. Ballesteros, J. Albaladejo and E. Jiménez, *ACS Earth Sp. Chem.*, 2019, **3**, 1873–1883.
34 B. R. Rowe, A. Canosa and D. E. Heard, *Uniform Supersonic Flows in Chemical Physics*, 2022.
35 J. Albaladejo, B. Ballesteros, E. Jiménez, Y. Díaz de Mera and E. Martínez, *Atmos. Environ.*, 2003, **37**, 2919–2926.
36 Y. Zhao and D. G. Truhlar, *J. Chem. Theory Comput.*, 2008, **4**, 1849–1868.
37 B. J. Lynch, Y. Zhao and D. G. Truhlar, *J. Phys. Chem. A*, 2003, **107**, 1384.
38 L. G. Gao, J. Zheng, A. Fernández-Ramos, D. G. Truhlar and X. Xu, *J. Am. Chem. Soc.*, 2018, **140**, 2906–2918.
39 M. Page and J. W. McIver Jr, *J. Chem. Phys.*, 1988, **88**, 922–935.
40 I. M. Alecu, J. Zheng, Y. Zhao and D. G. Truhlar, *J. Chem. Theory Comput.*, 2010, **6**, 2872–2887.
41 M. J. Frisch, G. W. Trucks, H. B. Schlegel, G. E. Scuseria, M. A. Robb, J. R. Cheeseman, G. Scalmani, V. Barone, G. A. Petersson, H. Nakatsuji, X. Li, M. Caricato, A. V. Marenich, J. Bloino, B. G. Janesko, R. Gomperts, B. Mennucci, H. P. Hratchian, J. V. Ortiz, A. F. Izmaylov, J. L. Sonnenberg, D. Williams-Young, F. Ding, F. Lipparini, F. Egidi, J. Goings, B. Peng, A. Petrone, T. Henderson, D. Ranasinghe, V. G. Zakrzewski, J. Gao, N. Rega, G. Zheng, W. Liang, M. Hada, M. Ehara, K. Toyota, R. Fukuda, J. Hasegawa, M. Ishida, T. Nakajima, Y. Honda, O. Kitao, H. Nakai, T. Vreven, K. Throssell, J. Montgomery, J. A., J. E. Peralta, F. Ogliaro, M. J. Bearpark, J. J. Heyd, E. N. Brothers, K. N. Kudin, V. N. Staroverov, T. A. Keith, R. Kobayashi, J. Normand, K. Raghavachari, A. P. Rendell, J. C. Burant, S. S. Iyengar, J. Tomasi, M. Cossi, J. M. Millam, M. Klene, C. Adamo, R. Cammi, J. W. Ochterski, R. L. Martin, K. Morokuma, O. Farkas, J. B. Foresman and D. J. Fox, *Gaussian, Inc., Wallingford, CT*, 2016.
42 F. Neese, F. Wennmohs, U. Becker and C. Riplinger, *J. Chem. Phys.*, 2020, **152**, 224108.
43 D. Ferro-Costas, D. G. Truhlar and A. Fernández-Ramos, *Comput. Phys. Commun.*, 2020, **256**, 107457.
44 Y. Georgievskii and S. J. Klippenstein, *J. Chem. Phys.*, 2005, **122**, 194103.
45 A. Fernández-Ramos, A. Ellingson, B. C. Garrett and D. G. Truhlar, *Rev. Comput. Chem.*, 2007, **23**, 125.
46 A. Fernández-Ramos, B. A. Ellingson, R. Meana-Pañeda, J. M. C. Marques and D. G. Truhlar, *Theor. Chem. Acc.*, 2007, **118**, 813–826.
47 W. Siebrand, Z. Smedarchina, E. Martínez-Núñez and A. Fernández-Ramos, *Phys. Chem. Chem. Phys.*, 2016, **18**, 22712–22718.
48 B. A. Ellingson, V. A. Lynch, S. L. Mielke and D. G. Truhlar, *J. Chem. Phys.*, 2006, **125**, 084305.
49 A. Fernández-Ramos, *J. Chem. Phys.*, 2013, **138**, 134112.